Experimental Thermal and Fluid Science 155 (2024) 111181

Contents lists available at ScienceDirect

Experimental Thermal and Fluid Science

journal homepage: www.elsevier.com/locate/etfs

Ice accretion characteristics on rotating aeroengine fan blades

Linchuan Tian, Haiyang Hu, Ramsankar Veerakumar, Hui Hu *

Dept. of Aerospace Engineering, Iowa State University, Ames, IA, USA

ARTICLE INFO

Keyword:
Aeroengine Icing pheomena
Quantification of 3D shapes of iced blades
Icing induced performance degradation of fan rotor

ABSTRACT

An experimental study was conducted to characterize the dynamic ice accretion process on rotating aero-engine fan blades to evaluate the icing-induced detrimental effects on the fan rotor performance. A scaled spinner-fan model was installed in an Icing Research Tunnel and exposed to typical rime and glaze icing conditions. It was found that, while ice structures accreted on both the suction and pressure surfaces of the fan blades, more ice accumulated in the region near the blade roots than those near the blade tips. The ice structures accreted on the fan blades not only deteriorated the shapes of the deliberately designed blades greatly but also blocked the airflow passages through the fan rotor substantially, regardless of the icing type. More specifically, the thickness of the fan blades was found to increase up to 40 % after undergoing 480 s of the rime icing experiment, the airflow passages were blocked by up to 14 % due to the rime ice accretion near the blade roots, resulting in about 70 % reduction of the air pressure increment across the fan rotor. Due to the combined effects of the aerodynamic shear forces and centrifugal forces associated with the rotating motion, substantial water runback was observed over the rotating blade surfaces under the glaze icing condition, resulting in the rapid growth of more complex "needle-like" icicles along the blade leading edges. Glaze ice accretion was found to cause more serious and faster performance degradation to the fan rotor than the rime icing scenario. While the airflow passages between the neighbouring blades were blocked by up to 18 % after undergoing 120 s of the glaze icing experiment, the airflow was found to be depressurized, instead of pressurized, after passing the iced fan rotor.

1. Introduction

Aircraft icing is a significant hazard to aviation safety in cold weather. Ice may accrete on every exposed airframe surface, including wings, propellers, antenna, and windshields. Ice accretion would deteriorate the deliberately designed shapes of the key components, leading to performance degradation of the airplane substantially (i.e., increasing aerodynamic drag while decreasing the lift dramatically) [1–3]. Ice can also accrete on the exposed surfaces of aero-engines, such as inlet lips, spinners, and fan blades, to cause serious detrimental effects on the aeroengine performances [4–6]. For example, in addition to degrading the aerodynamic performances, randomly accreted ice structures over the rotating aero-engine spinners [7] and fan blades [8] would also result in an imbalance of the rotating system, leading to serious mechanical vibrations [9]. Meanwhile, the shedding of large ice chunks from engine lips, rotating spinner, and fan blades could damage the engine casing, compressor cascade, and other downstream components, causing "power-loss" accidents such as stall, surge, and flameout [10]. While extensive studies have been performed in recent years to investigate aircraft icing physics and to develop effective anti-/de-icing strategies for aircraft icing protection [11–13], the focus of those studies concentrated primarily on icing process over fixed aircraft wings. The investigations on aero-engine icing phenomena are very limited, especially about the ice accretion characteristics on rotating fan blades [14–18]. Due to the more complicated shapes of the twisted and curved fan blades, the intricated internal flow environment with substantial pressure gradient and the additional effects of centrifugal forces associated with the rotating motion, the characteristics of the ice accretion process on rotating fan blades would become much more complex than that on fixed aircraft wings.

Most previous studies to examine icing phenomena on aero-engine fan blades were based on numerical simulations. Das et al. [19,20] conducted a series of numerical studies to examine the characteristics of ice accretion on the fan blades of a high bypass turbofan engine. Hutchings et al. [21] integrated various icing simulation tools to characterize the shape changes of fan blades due to ice accumulation and examined the icing-induced performance degradation. They reported that, for the test case with the accreted ice layer thickness being ~ 8 % of

* Corresponding author.
E-mail address: huhui@iastate.edu (H. Hu).

https://doi.org/10.1016/j.expthermflusci.2024.111181
Received 7 October 2023; Received in revised form 31 January 2024; Accepted 8 March 2024
Available online 11 March 2024

the blade chord length, icing-induced pressure loss was tripled, and the rate of the airflow inhaled by the fan blades was reduced by 15 %, in comparison to the case without any ice accretion. Bidwell et al. [22] used NASA's LEWICE3D software to simulate the ice accretion process on an Energy Efficient Engine (E3). They found that supercooled water droplets with larger droplet sizes resulted in an increased impingement rate on the fan blades. More recently, Dong et al. [23] examined the ice accretion characteristics on rotating aero-engine fan blades numerically. The characteristics of ice accretion on rotating fan blades were quantified by comparing the profiles of the iced blade at different spanwise positions. While the findings derived from those numerical studies are helpful to understand the characteristics of the ice accretion process on rotating fan blades, more experimental investigations are still highly desirable to gain further insight into the underlying physics pertinent to aero-engine icing phenomena. Furthermore, the quantitative measurement results are needed to establish comprehensive experimental databases to validate/verify numerical simulations and theoretical modelling of the ice accretion characteristics on rotating fan blades.

A comprehensive experimental campaign is conducted in the present study to characterize the dynamic ice accretion process on rotating aero-engine fan blades and to quantify the icing-induced performance degradation to the fan rotor. The experimental study is conducted in the Icing Research Tunnel at Iowa State University (i.e., ISU-IRT) with a scaled aero-engine spinner-fan model exposed to typical wet glaze and dry rime icing conditions. During the experiment, while the dynamic ice accretion process over the rotating fan blades was recorded by using high-resolution imaging systems along with a phase-locking technique, a 3D profile scanning system was also utilized to quantify the 3D shape changes of the iced fan blades as a function of the ice accreting time. The time evolutions of the air pressure increment across the fan rotor were also monitored to evaluate the icing-induced performance degradation of the fan rotor. The primary objective of the present study is to quantify the characteristics of the ice structures accreted on rotating fan blades and the icing-induced performance degradation of the fan rotor under various icing conditions. The quantitative measurement results derived from the present study may also be used to validate/verify numerical simulations and theoretical models to predict the dynamic ice accretion processes on rotating fan blades.

2. Experimental setup and test model

2.1. Icing research tunnel used for the present study

The experimental study was performed in the Icing Research Tunnel of Iowa State University (i.e., ISU-IRT). As shown schematically in Fig. 1, the ISU-IRT has a transparent test section of 400 mm in width, 400 mm in height, and 2,000 mm in length. It has the capacity to generate an icing environment with a maximum wind speed (i.e., V_∞) of 60 m/s and temperature (i.e., T_∞) down to −20 °C. 9 pneumatic spray atomizers/nozzles (IKEUCHI-BIMV-8002) were installed to inject micro-sized water droplets into the airflow in the ISU-IRT. The liquid water content (LWC) level in the ISU-IRT can be adjusted from LWC = 0.1 g/m^3 to 6.0 g/m^3 by manipulating the working parameters of the spray nozzles. Based on the measurement results using a LaVision's ParticleMaster^{TM} system, the water droplets exhausted from the spray nozzles were found to be 10 to 100 μm in size with the mean volume diameter (MVD) of the water droplets being about 20 μm[24]. At the given icing conditions, the temperature fluctuations within the test section of ISU-IRT was found to be within ± 1.0 °C. By leveraging the ISU-IRT, extensive studies have been conducted in recent years to investigate various atmospheric icing phenomena [17,25–28].

2.2. The test model used in the present study

An aero-engine spinner-fan model used in the present study was designed based on a Boeing 18-inch aero-engine test rig [29,30] with a scale ratio of 1:2.3. The schematic of the fan blade is presented in Fig. 2. The design rotor pitches at 25 %, 50 %, and 75 % blade span are 18 mm,

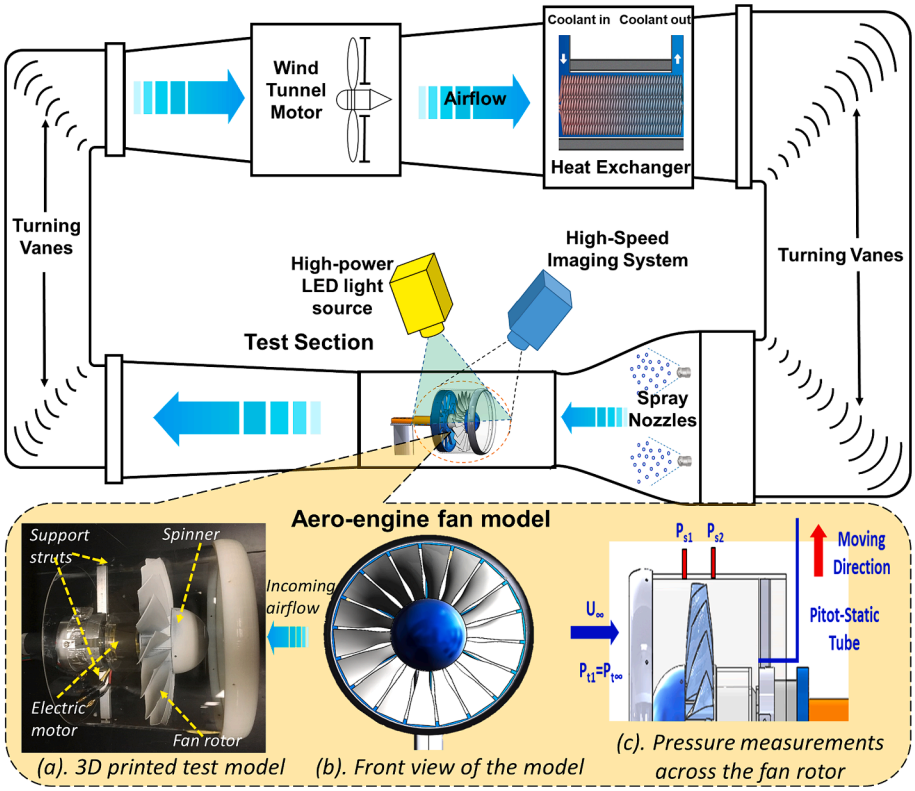

Fig. 1. ISU-IRT and the test model.

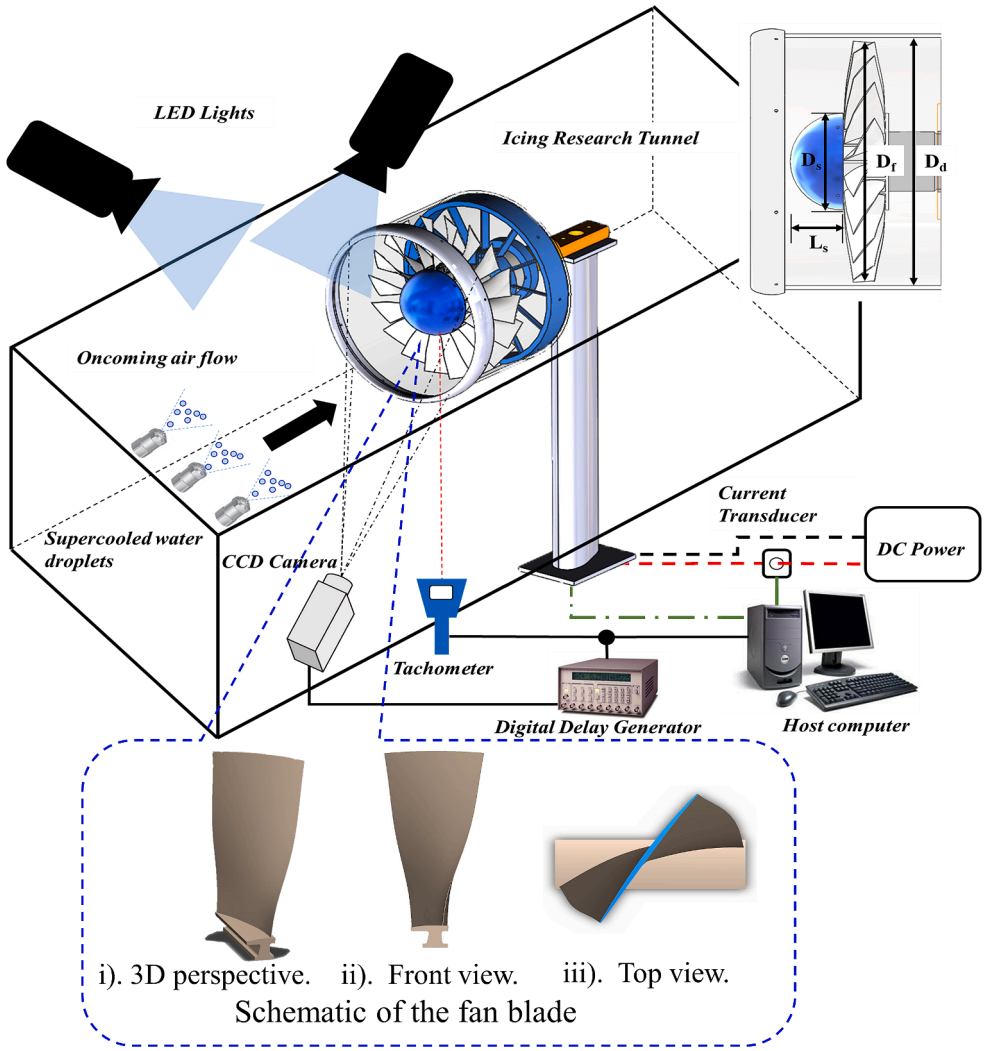

Fig. 2. Schematic of the experimental setup.

24 mm, and 34 mm, respectively. The hub/tip ratio is designed to be 0.402 with the aspect ratio being 1.65. Eighteen blades are installed circumferentially on a rotating fan disk with the outer diameter being 200 mm. The fan rotor has a solidity of 2.214 at the hub and 1.035 at the tip. An elliptical-shaped spinner was mounted in the front of the fan rotor, which has a length of $L_S = 40$ mm and base diameter of $D_S = 80$ mm. A rounded lip ring, a transparent cylindrical duct, and four struts were used to assemble an engine nacelle. The gap between the nacelle's inner wall and the rotating blade tips was set to be 1.0 mm. Further technical details of the designs of th fan blades and spinners can be found at Tian[31].

All the parts of the test model, except the transparent nacelle case, were manufactured by using a 3D printer (Connex 500 3D printer) with a hard-plastic material (VeroWhitePlus, Stratasys) with a thermal conductivity of 0.45 W/(m·K). The surfaces of the 3D-printed parts were polished with fine sandpapers. A commercially available Superhydrophobic coating (i.e., NeverWet^{TM} by Rust-Oleum®) was spray-coated over the spinner surface to minimize the ice accretion over the rotating spinner surface.

The rotation of the spinner-fan model was driven by a brushless motor (Scorpion, SII-4020-420KV), which is powered by a Direct Current (DC) power supply (BK PRECISION, 1692). An electrical speed controller (ESC, Scorpion, Commander 15 V 60A), a Proportional-Integral-Derivative (PID) feedback control module and a data acquisition system (NI, USB-6218) were used to enable the spinner-fan model to rotate at a pre-selected constant rotation speed during the icing experiments.

2.3. Selection of the test parameters and icing conditions

A kinematic similarity is used in the present study to determine the operational parameters of the spinner-fan model to simulate the operation condition of a typical CFM56-2/3 turbofan engine which has an advance ratio $J = \frac{V_\infty}{\pi \cdot \Omega \cdot D_{fan}} = 1.8$, where V_∞ is the incoming flow speed, Ω is the rotation speed, and D_{fan} is the diameter of the fan rotor. While the incoming airflow velocity in ISU-IRT was set to be $V_\infty = 15$ m/s during the icing experiments, the spinner-fan model rotated with a constant angular velocity of $\Omega = 2{,}500$ rpm. As a result, the spinner-fan model would have the same advance ratio of $J = 1.8$ as the prototype engine.

It Is well known that supercooled water droplets would be frozen into ice immediately upon the impingement onto a solid surface. The freezing can be finished completely or partially, depending on how rapidly the latent heat of fusion can be released into the ambient airflow [32–34]. In a dry regime, all the supercooled water collected in the impingement area would freeze instantly upon impact to form *rime ice*. For a wet regime, only a fraction of the impinged supercooled water droplets would freeze in the impingement area to form *glaze ice* and the remaining unfrozen water would run back and freeze subsequently outside the direct impingement zone of the droplets. *Mixed ice* refers to the situation with a simultaneous appearance of both *rime* and *glaze* ice

characteristics.

In the present study, the key parameters for the icing experiments were selected by following the guidance of the Airworthiness Standard of Title 14 of FAA for the Code of Federal Regulations (CFR) in Appendix C CM and IM conditions in general. Typical rime and glaze icing conductions were generated by adjusting the liquid water content (LWC) levels and temperature of the incoming airflow in the test section of ISU-IRT. More specifically, while the test parameters of $V_\infty = 15$ m/s, LWC $= 0.50$ g/m^3 and $T_\infty = -15$ ℃ were selected for the rime icing experiment, the parameters were set to $V_\infty = 15$ m/s, LWC $= 2.0$ g/m^3 and $T_\infty = -5$ ℃ for the glaze icing experiment, and the MVD (Mean Volume Diameter) was set as 20 μm during all the test cases by adjusting the air/water pressure ratio supplied to the water spray system of ISU-IRT.

Following the work of Anderson [35], an icing similarity parameter, named ice accumulation parameter, is used to in the present study to compare the ice accretion characteristics on the rotating fan blades under different icing conditions. The ice accumulation parameter, A_c, is defined as:

$$A_c = \frac{LWC \cdot V_\infty \cdot t}{\rho_{ice} \cdot l} \tag{1}$$

where LWC LWC refers to the liquid water content in the incoming airflow; V_∞ V_{rel} is the incoming airflow velocity; t t is the ice accretion time; ρ_{ice} is the ice density; and l is the characteristic length of the test model (e.g., the maximum thickness of the blade). As given in Equation (1), for the same incoming airflow velocity and the same spinner-fan model used in the present study, the value of the ice accumulation parameter of A_C A_c would vary linearly with LWC value and the ice accretion time, t.

Since the LWC level in the incoming airflow for the *rime* icing case (i.e., $LWC = 0.50$ g/m^3) is much smaller than that of the *glaze* icing case (i.e., $LWC = 2.0$ g/m^3), the duration of the rime icing experiments (i.e., total duration of ~ 480 s) was set to be 4.0 times of the glaze icing experiments (i.e., total duration of ~ 120 s) to ensure the same value of the ice accumulation parameter based on the Equation (1).

2.4. Measurement systems used for the icing experiments

As shown schematically in Fig. 2, the dynamic ice accretion process on the rotating fan blades was recorded using two sets of imaging systems (i.e., FASTCAM MINI WX cameras with 2048 pixels × 2048 pixels spatial resolution) along with Nikon lenses (50 mm 1.8D and 105 mm NIKKOR 1.4E ED lenses). While one of the imaging systems was set to have a larger observation window (i.e., 300 mm by 300 mm) to reveal the global features of the ice accretion process, the second system focused on a pre-selected fan blade to provide a "zoom-in" view (i.e., 100 mm by 100 mm in size) to reveal further details of the icing process. The two imaging systems were synchronized for the imaging acquisition. During the experiment, the rotation speed of the spinner-fan model was monitored by using a digital tachometer (MONARCH PLT200), which can generate a pulsed Transistor-Transistor-Logic (TTL) signal from each rotation cycle. The pulsed TTL signal was then sent to a Digital Delay Generator (BNC Model577) to trigger the two imaging systems to achieve "phase-locked" image acquisition to reveal the dynamic ice accretion process over the surface of the same fan blade. A uniform, low-flicker illumination was provided using a pair of 200 W studio light-emitting diode (LED) lights for the ice accretion image acquisition. With the experimental setup shown in Fig. 2, only the ice structures accreted on the suction-side surfaces of the fan blades can be recorded using the imaging systems.

In addition to acquiring the "phase-locked" images to record the dynamic ice accretion process over the rotating fan blades, a novel digital image projection (DIP) based 3D profile scanning system was also used to quantify the 3D shape changes of the fan blades due to the ice accretion. The DIP technique is based on a working principle of structured light triangulation, similar to the stereo version measurement technique, where one camera is replaced with a digital projector[36]. During the measurement, an image pattern (e.g., mesh or triangle pattern) with known statistics is projected onto the object surface of interest (i.e., a fan blade for the present study). After the ice accumulates on the blade surface, the projected digital pattern would be distorted in the view of the camera (i.e., shown as the distorted pattern in the acquired image), in comparison to the ice-free pattern (i.e., the reference pattern). By comparing the distorted pattern with the reference image, the 3D shape of the iced blade can be reconstructed quantitatively by leveraging a pre-calibration parameter matrix. The same DIP system has been used recently to measure 3D-printed hemispherical roughness elements on a test plate for the measurement accuracy estimation[37]. Based on the measurements of about 500 points around given hemispherical roughness elements with a nominal height of 8.0 mm, the measurement uncertainty of the DIP system was found to be about 150 μm, i.e., ~ 2.0 % of the targeted heights of the measurements. Further information about the technical basis, system setup, and calibration procedure for the 3D shape measurements of iced test models using the DIP-based 3D profile scanning technique is available in our previous studies [24,37]. As an optical-based, non-intrusive measurement technique, the DIP-based 3D profile scanning technique can measure the 3D shapes of iced fan blades without damaging the fragile ice structures, which offers significant advantages over the conventional labor-intensive methods, such as hand tracing and mold-and-casting methods.

Fan blades are designed to compress the airflow and guide the air streams flowing smoothly into the engine core. A higher air pressure increment passing the fan rotor would not only lead to a stronger thrust force for the bypass airstreams but also result in a greater compression ratio of the engine core for better engine efficiency. As shown in Fig. 1 (c), two pressure tap arrays were manufactured on the nacelle to quantify the air pressure increment across the fan rotor. A digital pressure sensor array (i.e., DSA-3217 Scanivalve^{TM}) was connected to the pressure taps for the air pressure measurements, which has a pressure measurement range of 10-inch H_2O and ± 0.2 % in measurement accuracy. Measured pressure increments across the fan rotor were used to characterize the performance degradation of the fan rotor induced by the ice accretion.

3. Experimental results and discussions

3.1. Characteristics of dynamic ice accretion process on the rotating fan blades and the performance degradation to the fan rotor under the rime icing condition

Before conducting the icing experiments, the ISU-IRT was operated at a pre-scribed frozen cold temperature level (i.e., $T_\infty = -5.0\,^\circ C$ for the glaze icing experiments and $T_\infty = -15.0\,^\circ C$ for the rime icing experiments) for at least 30 min under a dry airflow condition (i.e., without turning on the water spray nozzles) to enable the system reaching a thermally steady state. Then, the water spray nozzles were switching on to inject micro-sized water droplets into the ISU-IRT. The tiny water droplets would be cooled down rapidly to reach a supercooled state. Upon impacting to the rotating fan blades, the impinged supercooled water droplets would be frozen into ice rapidly to start the ice accretion. As aforementioned, the freezing can be completely or partially, depending on how rapidly the latent heat of fusion can be released into the ambient airflow [32–34].

Fig. 3 shows "phase-locked" ice accretion images acquired under the rime icing condition. The image pairs acquired by using the two synchronized imaging systems reveal both the global and detailed features of the ice accretion on the suction-side of the blades. Since the released latent heat of fusion was dissipated rapidly under the rime icing condition with very cold ambient temperature of $T_\infty = -15$ ℃[38], the impinged supercooled water droplets were found to be frozen into ice instantly upon impacting the fan blades. The sites of the rime ice

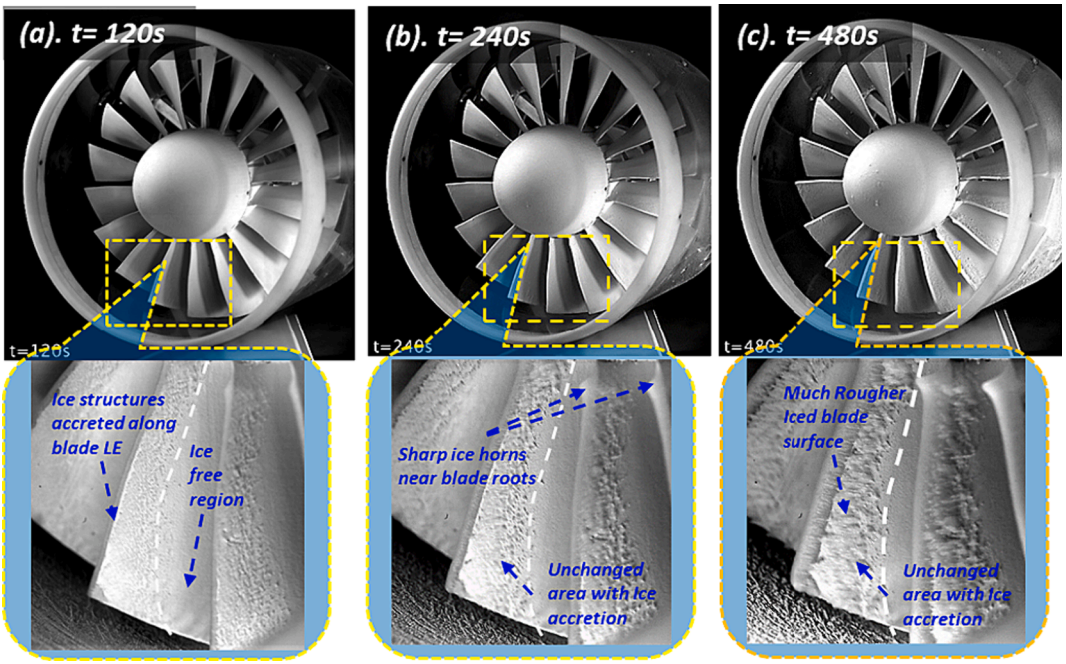

Fig. 3. Acquired ice accretion images under the rime icing condition.

accretion were determined primarily by the impinging characteristics of the airborne water droplets[39]. As revealed in Fig. 3, the accreted ice structures were opaque with a milky-white appearance, which is a typical feature of rime ice due to the entrainment of air bubbles/pockets between rime ice grains. The rime ice structures were found to accrete within the narrow regions near the blade leading edges, correlating well with the direct impinging zones of the airborne supercooled water droplets.

With more and more supercooled water droplets impinging onto the blade surfaces, the thickness of ice layers accreted over the blade surfaces increased monotonically with the ice accretion time. While the blade surfaces were found to become much rougher, the coverage of the ice layers accreted on the blade surfaces was found to be almost unchanged during the rime icing experiment (e.g., illustrated by the dashed lines given in the images). Because of the effects of the elliptical-shaped spinner on the flying trajectories of the airborne water droplets over the spinner surface[8], sharp ice horn structures were found to form near the blade roots. Since all the impinged water droplets were frozen into ice instantly under the rime icing condition, no traces of unfrozen water runback were observed in the ice accretion images.

The ice accretion characteristics over the rotating fan blades were revealed more clearly from the measured 3D shapes of the iced blades given in Fig. 4. It can be seen that, while ice structures were found to accrete on both the suction-side and pressure-side surfaces of the fan blades, ice accretion features on the suction-side were significantly different from those on the pressure-side, due to the different impinging characteristics of the airborne water droplets on the blade surfaces. As revealed in Fig. 4(a), since the direct impingement zone of the airborne water droplets on the suction-side surface of the blade was limited within a narrow region near the leading edge, the accreted ice structures were confined primarily along the blade leading edge with almost no ice accretion at further downstream locations on the suction-side surface. The 3D profile scanning results also confirmed quantitatively that, while the surfaces of the iced blade became rougher and rougher with the increasing ice accretion time, the coverage of the accreted ice layer on the suction-side of the blade was almost unchanged during the entire rime icing experiment.

Fig. 4(b) gives the front view of the iced fan blade, which reveals the time evolution of the ice structures accreted along the blade leading edge. The ice layer accreted around the blade leading edge was found to become much thicker and rougher with the increasing ice accretion time. The ice structures accreted around the leading edge extruded outward against the incoming airflow, which would intercept more airborne supercooled water droplets to accelerate the growth of the ice layer accreted along the blade leading edge.

As shown in Fig. 4(c), a rather non-uniform ice mass was found to accrete on the pressure side of the blade along the span direction. Much more ice was found to accrete near the root region on the pressure-side of the blade than those on the suction-side surface. While the twisted geometry and the mounting angle of the fan blades would lead to a shadow region near the blade tip on the pressure side where the airborne supercooled water droplets would not be able to impinge directly upon. Meanwhile, the rapid growth of the ice structure accreted alone the blade leading edge would extrude further into the incoming airflow to prevent the supercooled water droplets from impinging onto the blade surface. As a result, an almost “ice-free” zone was found to form in the region near the blade tip behind the iced blade leading edge on the pressure-side surface. For the rest of the pressure-side surface, since airborne supercooled water droplets would impinge directly onto the blade surface, the coverage of the accreted ice layer was found to extend from the blade leading edge all the way to the trailing edge, especially in the region near the blade root. Due to the direct impingement of more airborne supercooled water droplets, a thicker ice layer accreted in the region near the blade root on the pressure-side surface.

Based on the 3D scanning results given in Fig. 4, the profiles of the iced fan blade at 3 selected cross-sections were extracted (i.e., at 25 %, 50 %, and 75 % span away from the blade root, respectively), which are shown in Fig. 5. More interesting features of the rime icing process on the rotating blade were revealed based on the comparison of the measured profiles of the iced fan blade after undergoing different periods of the icing experiment. As revealed from the measured ice layer profiles at 75 % blade span, more ice structures were found to accrete near the blade leading edge on the suction-side surface of the blade (i.e., a thicker ice layer with a larger coverage) than those on the pressure-side surface. Corresponding to the highest water collection efficiency at the blade leading edge, the ice layer accreted at the leading edge had the fastest growth rate with the increasing ice accretion time. It can also be seen that the outer contour lines of the ice structures accreted near

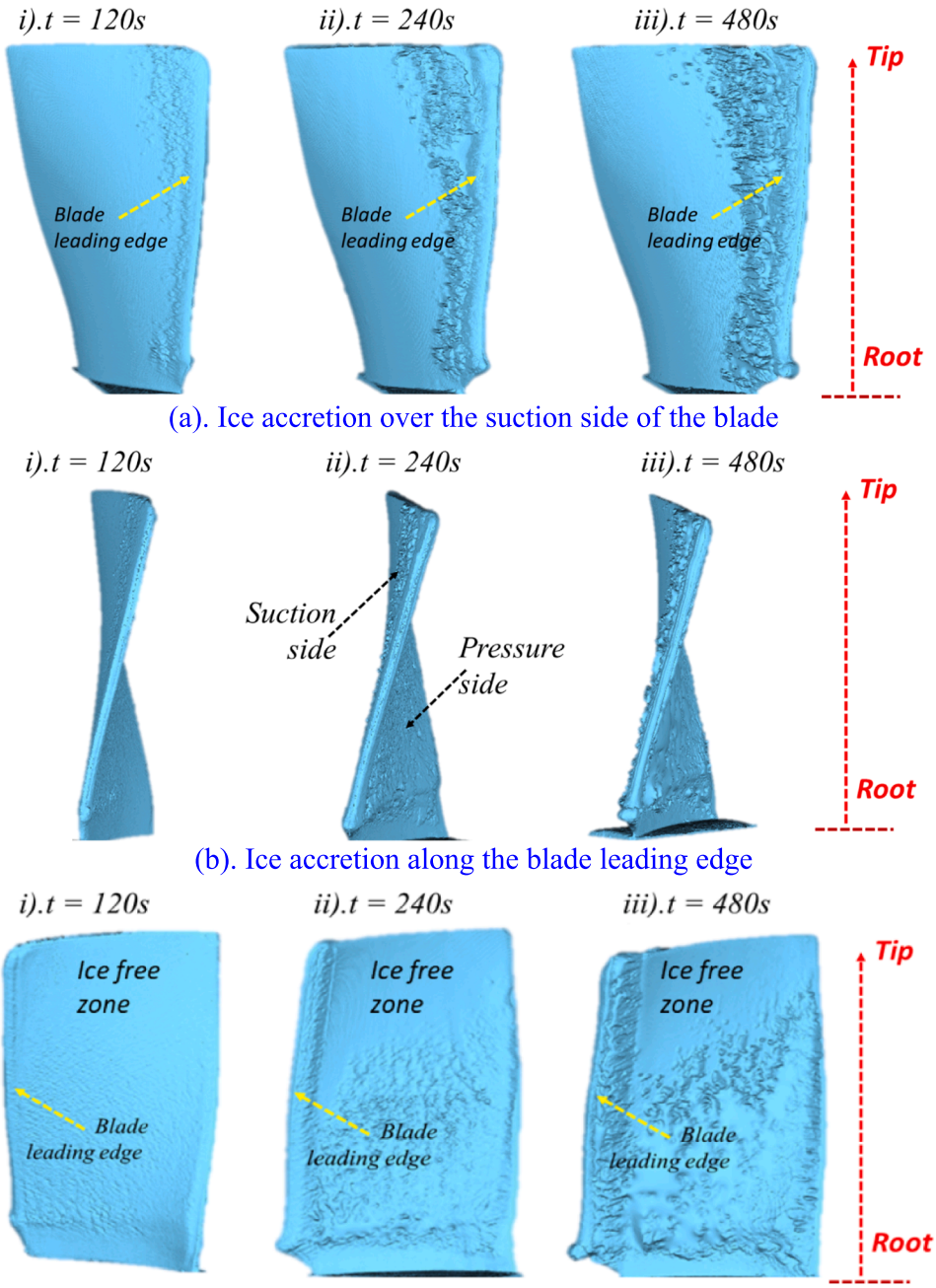

Fig. 4. Measured 3D shapes of the iced fan blade under the rime icing condition.

the blade leading edge on the pressure side for the $t = 240$ s case (i.e., the red line) were outside of those of $t = 480$ s case (i.e., the black line), suggesting that some of the ice structures accreted near the blade leading edge were actually shed off from the blade surface due to the combined effects of the aerodynamic shear forces exerted by the incoming airflow and the centrifugal forces associated with the rotating motion.

It should also be noted that the rapid growth of the ice accretion around the blade leading edge would not only induce large-scale airflow separation but also block the airflow passing through the fan rotor, resulting in substantial performance degradation to the fan rotor. More specifically, with the fast growth of the irregular-shaped ice structures accreted around the blade leading edge in the cross-section of 75 % blade span, the effective chord length of the iced fan blade was found to be increased by 15.7 % after undergoing the rime icing experiment for 480 s, causing the airflow passage between the fan blades reduced by 8.8 %. It can also be seen that, while the surface near the blade trailing edge was ice-free on the suction side, a small amount of ice structures was found to accrete near the blade trailing edge on the pressure side surface due to the direct impingement of airborne supercooled water droplets onto the region. As a result, the airflow passage near the blade trailing edge was reduced by 2.3 % near the blade trailing edge.

In comparison to those accreted near the blade tip, more ice structures were found to accrete over the pressure-side surface at the blade mid-span, leading to a thicker ice layer accreted on the pressure-side surface of the blade, as revealed by the measured contour lines of the iced fan blade at 50 % span. The rapid growth of the irregular-shaped ice structures was found to cause the effective chord length of the iced blade

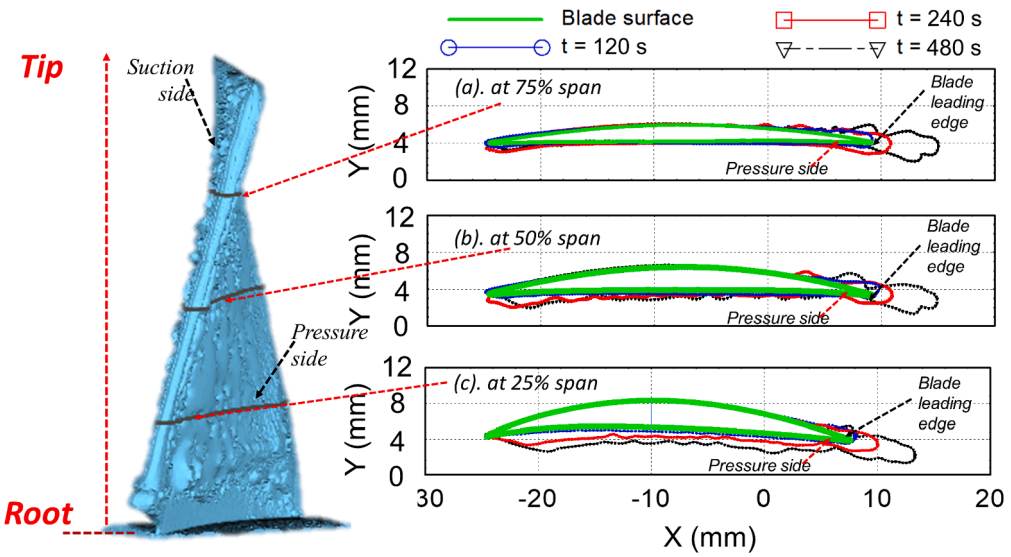

Fig. 5. Extracted profiles of the iced fan blades at three spanwise locations under the rime icing condition.

increased by 16.1 % near the leading edge after undergoing 480 s of the rime icing experiment, leading to the airflow passage between the fan blades reduced by 12.3 %. While rime ice structures were found to accrete over the entire pressure-side surface of the blade, the maximum thickness of the accreted ice layer was observed at the 85 % chord of the blade (i.e., up to ~ 20 % thicker), causing serious deformations from the deliberately design profile of the fan blade with much rougher surface. The icing-induced reduction of the airflow passage between the blades was found to be up to 8.3 % near the blade trailing edge at the midspan.

The ice structures accreted over the pressure-side surface in the region near the blade root (e.g., at 25 % span) caused the outer profile of the iced blade deviating significantly from the original profile of the blade (i.e., a completely different thickness distribution pattern with much rougher blade surface). The effective chord length of the iced blade was found to increase 14 % at the 25 % span after undergoing 480 s of the rime icing experiment. While the iced blade was found to become up to 40 % thicker due to the ice accretion, the airflow passage between the fan blades was blocked by 11 % and 14 % in the region near the leading and trailing edges of the blade, respectively. It is obvious that the characteristics of the air streams flowing through the fan rotor would be changed greatly due to the ice accretion, which was found to cause substantial detrimental effects on the performance of the fan rotor.

In the present study, a non-dimensional parameter, named air pressure increment coefficient, $C_{\Delta p}$, is used to characterize the performance of a fan rotor[8], which is expressed as:

$$C_{\Delta P} = \frac{\Delta P}{\frac{1}{2}\rho_{air} V_{\infty}^2} = \frac{P_{s2} - P_{s1}}{\frac{1}{2}\rho_{air} V_{\infty}^2} \quad (1)$$

where P_{s2} and P_{s1} are the measured air pressure across the fan rotor. The V_{∞} and ρ_{air} are the airflow velocity and density. Since the fan rotor is supposed to compress air streams, the air pressure is expected to increase after the airflow passes the fan rotor (i.e., $P_{s2} > P_{s1}$). With the test parameters used in the present study, the air pressure increment coefficient of the fan rotor was measured to be 0.11 (i.e., $C_{\Delta P,ice\text{-}free} \approx 0.11$) under an ice-free condition.

While the fan rotor was set to rotate with a constant angular speed of Ω = 2,500 rpm during the icing experiments, the pressure increment coefficient of the fan rotor was measured to quantify the icing-induced performance degradation. To better illustrate the detrimental effects of the ice accretion on the fan rotor performance, the normalized pressure increment ratio (i.e., NPIR in short) of the fan rotor is introduced, which is defined as:

$$NPIR = \frac{C_{\Delta P,iced}}{C_{\Delta P,ice-free}} \quad (2)$$

where $C_{\Delta p,ice\text{-}free}$ and $C_{\Delta p,iced}$ are the pressure increment coefficients of the fan rotor before and after starting the icing experiments.

Fig. 6 shows the variations of the measured NPIR value of the fan rotor as a function of the ice accretion time under the rime icing condition. It can be seen that the measured NPIR value was found to increased gradually initially, reached its maximum at the time of $t \approx 90$ s, then decreased monotonically with the increasing ice accretion time. Such an interesting feature is closely related to the characteristics of the rime ice accretion process on the fan blade.

Since the impinged supercooled water droplets would be frozen into ice instantly under the rime icing condition, the rime ice structures accreted on both the suction and pressure surfaces of the fan blades would follow the original shape profiles of the blades in general at the initial icing stage. The rime ice grains accreted over the blade surfaces would make the surfaces much rougher than those without the ice accretion. The roughness build-up at the beginning of the rime icing process would act as "turbulators" to promote a fast transition of the laminar boundary airflows over the fan blades [40], thereby, improving the aerodynamic performance of the fan blades. Meanwhile, the ice layers accreted around the blade leading and trailing edges would increase the effective chord lengths of the fan blades, which would also contribute to the improved air pressure increment of the fan rotor at the initial stage of the rime icing process.

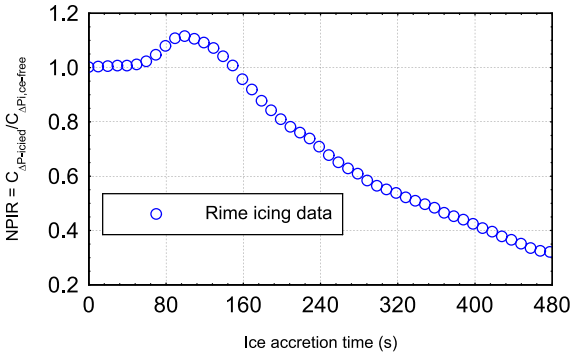

Fig. 6. The measured NPIR value of the fan rotor under the rime icing condition.

However, with more and more rime ice structures accreted on the fan blades at the later stage of the rime icing process, while the blade surfaces became much rougher, the outer profiles of the iced blades were found to deviate seriously from their original shapes. Furthermore, irregular-shaped ice structures were found to accrete along the blade leading edges, which would induce large-scale airflow separation on the blade surfaces to degrade their aerodynamic performance significantly. Furthermore, the continuous growth of the ice layers accreted over the blade surfaces was also found to block the passages of the airflow inhaled by the aeroengine, which would also degrade the performance of the fan rotor. Therefore, the NPIR value of the fan rotor was found to decrease monotonically with the increase ice accretion time, as shown in Fig. 6.

3.2. Characteristics of dynamic ice accretion process on the rotating fan blades and the performance degradation to the fan rotor under the glaze icing condition

Fig. 7 gives the "phase-locked" images acquired under the glaze icing condition. Many interesting features of the glaze ice accretion process were revealed from the time sequence of the acquired images. In comparison to the rime icing scenario described above, more airborne supercooled water droplets would impinge onto the blade surfaces within a unit time due to the higher LWC level in the airflow under the glaze icing condition (i.e., $LWC = 2.0\ g/m$), causing a much greater amount of the latent heat of fusion released over the blade surfaces associated with the solidification (i.e., icing) process. However, the heat transfer (i.e., both convective and conductive heat transfer) capacities under the glaze icing condition would become much weaker due to the higher ambient temperature (i.e., $T_\infty = -5.0$ ℃), which was insufficient to dissipate the released latent heat of fusion rapidly. As a result, only a fraction of the impinged water droplets was frozen into ice immediately with the rest fraction staying in liquid. The unfrozen impinged water would flow freely over the surfaces of the rotating blades until all the released latent heat of fusion was dissipated completely. Thus, transparent ice structures with glazy appearance were found to accrete over the surface of the fan blades, as revealed in Fig. 7.

Driven by the aerodynamic shear forces exerted by the incoming airflow, the unfrozen water would flow over the ice accreting blade surfaces, forming runback water flows to transport the unfrozen water collected in the region near the blade leading edge (i.e., within the direct impinging zone of the airborne water droplets) to further downstream locations. Interacting with the frozen-cold incoming airflow (i.e., $T_\infty = -5.0$ ℃), the runback water would be cooled down continuously, and frozen into ice eventually once the released latent heat of fusion was dissipated completely. As a result, the coverages of the ice layers accreted over the blade surfaces were found to increase continuously with the ice accretion time, as shown in Fig. 7.

It can also be seen that, because of the effects of the centrifugal forces associated with the rotating motion, the unfrozen water accumulated on the fan blades was also pushed to flow radially, leading to the unfrozen water flowing from the blade roots towards the blade tips. A fraction of the unfrozen water was even found to take off from the blade surfaces. Interacting with frozen cold airflow, the unfrozen water was cooled down continuously and frozen into ice eventually, leading to the rapid growth of "needle-like" icicle structures extruding outward against the incoming airflow. As revealed in Fig. 7(c), more "needle-like" icicles accreted in the outbound regions of the fan blades due to the stronger centrifugal forces associated with the larger rotation radius near the blade tips.

The characteristics of the glaze ice accretion process on the rotating fan blades were revealed more clearly from the 3D shapes of the iced blades presented in Fig. 8. It can be seen that substantial ice structures were found to accrete on both the suction and pressure surfaces of the fan blades. However, ice accretion characteristics under the glaze icing condition were found to become significantly different from those of the rime icing process due to the runback features of the unfrozen water on the rotating fan blades under the combined effects of the aerodynamic forces and the centrifugal forces.

Since only a portion of the supercooled water droplets would be frozen into ice immediately upon impacting the blade surface under the glaze icing condition, the rest of the impinged water droplets would flow freely on the surfaces of the rotating fan blades. The traces of the unfrozen water runback and subsequent ice accretion on the suction surface of the fan blade were revealed clearly in Fig. 8(a). Driven by the aerodynamic shear forces exerted by the incoming airflow, the unfrozen water was forced to flow away from the impinging sites near the blade leading edge to reach further downstream locations, causing the streamwise expansion of the ice coverage on the suction surface of the fan blade with the increasing ice accretion time. Meanwhile, the

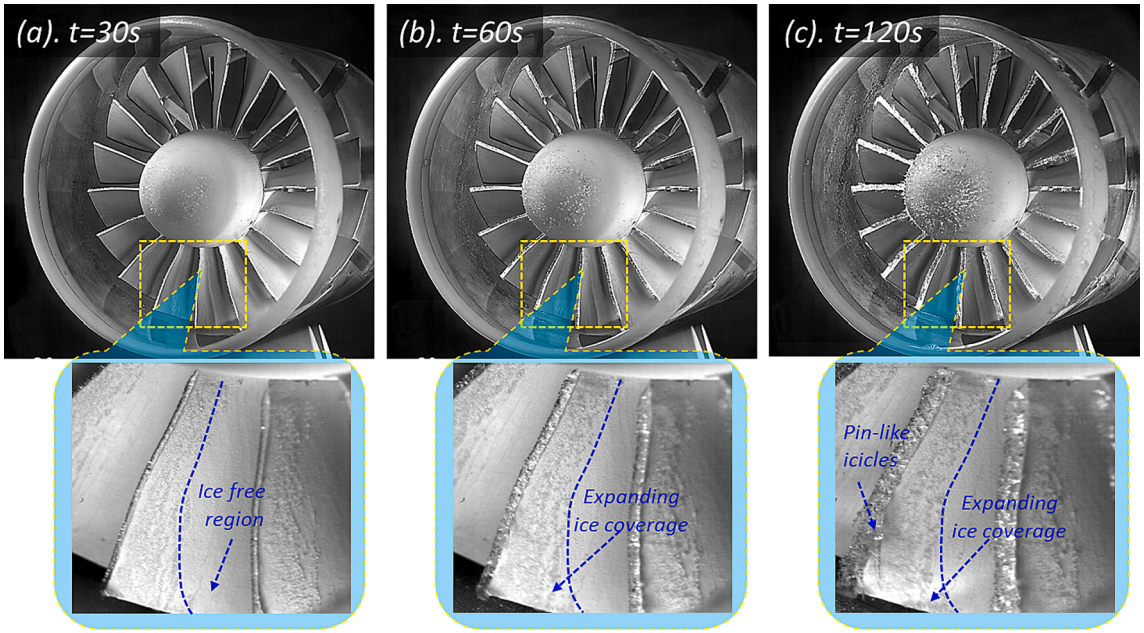

Fig. 7. Acquired ice accretion images under the glaze icing condition.

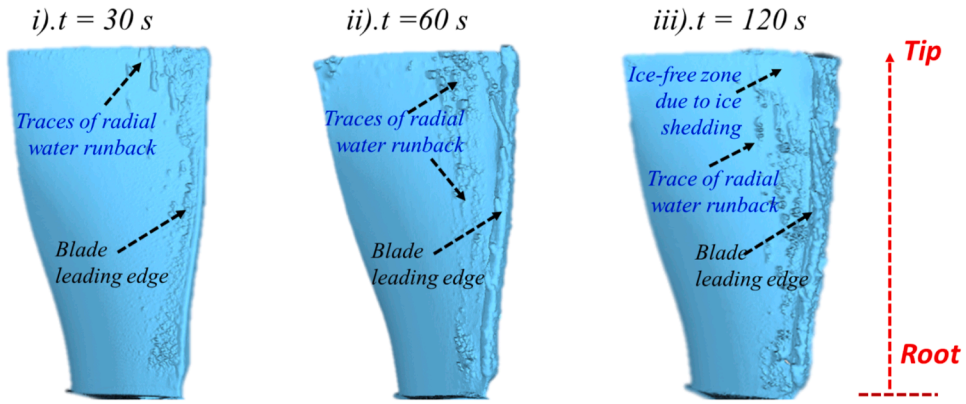

(a). Ice accretion over the suction side surface of the blade.

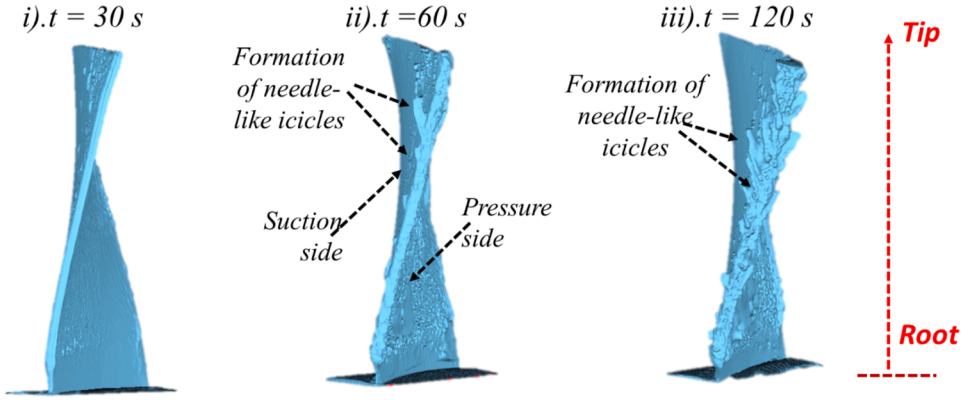

(b). Ice accretion along the leading edge of the blade.

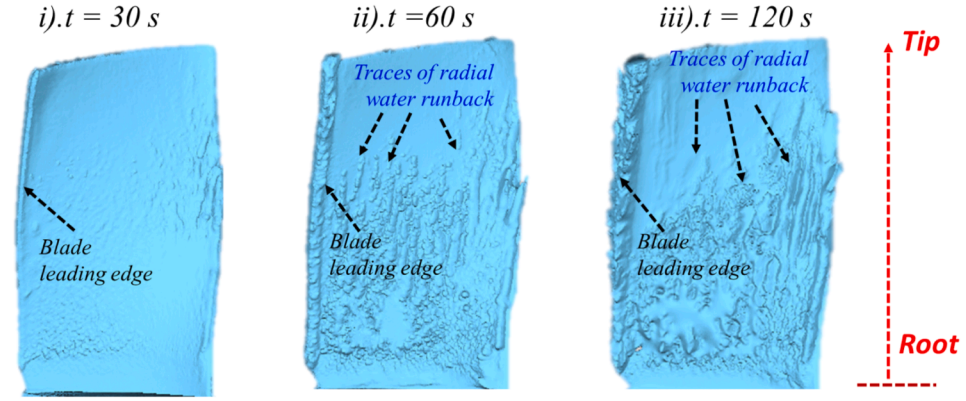

(c). Ice accretion over the pressure side surface of the blade.

Fig. 8. Measured 3D shapes of the iced fan blade under the glaze icing condition.

centrifugal forces associated with the rotating motion would push the unfrozen water flowing radially, leading to a wider ice coverage on the suction surface in the outbound region than those near the blade root. It can also be seen that, due to the stronger centrifugal forces near the blade tips, a fraction of the unfrozen water and/or accreted ice structures was found to shed off from the blade surface, causing the "ice-free zones" in the region near the blade tip, as shown in Fig. 8 (a).

As shown in Fig. 8(b), the ice structures accreted near the blade leading edge were found to have much more complex shapes under the glaze icing condition than those under the rime icing condition, which was closely related to runback characteristic of the unfrozen water over the ice accreting blade surface. Driven by the centrifugal force associated with the rotating motion, the unfrozen water collected near the blade leading edge would flow radially to transport the impinged water mass from the blade root toward the blade tip. Because of the stronger centrifugal force in the region near the blade tip, a portion of the unfrozen water was found to take off from the leading edge of the rotating blade and was frozen into ice subsequently while taking off, resulting in the formation of the very complicated, "needle-like" icicles extruding into the incoming airflow. More needle-like icicles were found to accrete along the blade leading edge with increasing ice accretion time, primarily in the outbound region, due to the greater centrifugal forces associated with the greater rotating radius. It should also be noted that, associated with the greater centrifugal forces near the blade tip, unfrozen water or/and the ice structures accreted near the blade tip were more readily to shed off from the rotating fan blades, causing the less ice

accretion near the blade tip, as shown in Fig. 8(b).

As revealed in Fig. 8(c), corresponding to the much wider direct impinging zone of the airborne water droplets on the pressure side of the fan blade, more ice accreted on the pressure side than the suction side of the fan blade, resulting in the accreted ice layer extending from the blade leading edge all the way to the trailing edge. While more ice structures were found to accrete in the region near the blade root than those near the blade tip, the traces of radial water runback driven by the centrifugal force were also revealed very clearly. Similar as that described above, associated with the much stronger centrifugal force near the blade tip, unfrozen water and accreted ice structures would be more readily to shed off from the blade surface in the region near the blade tip, resulting in the "ice free" zone near the blade tip on the pressure side of the blade surface.

Fig. 9 presents the extracted profiles of the iced fan blade in 3 selected cross-sections (i.e., at 25 %, 50 %, and 75 % blade span) based on the measurement results given in Fig. 8. It should be noted that, after 120 s of the glaze icing experiment, the value of the ice accumulation parameter as defined in Eqn. (1) would have the same value as that after 480 s of the rime icing experiment. It indicates that the fan blade would be exposed to the impingement of almost same amount of airborne supercooled water droplets. As revealed quantitatively in Fig. 9(a), the coverages of ice layers accreted on the fan blade (i.e., on both suction and pressure surfaces) under the glaze icing condition were smaller in the region near the blade tip (i.e., at 75 % span) than those accreted under the rime icing condition. This is believed to be closely related to the more readily shedding-off the accreted ice structures from the rotating fan blade under the glaze icing condition. The ice adhesion strength to the same fan blade is known to be weaker at a warmer temperature. Because of the stronger centrifugal force near the blade tip, the accreted ice under the glaze icing condition (i.e., $T_\infty = -5.0$ ℃) would be more readily shed off from the blade than those of the rime icing case (i.e., $T_\infty = -15.0$ ℃), causing the less ice accreted on the blade surface under the glaze icing condition.

However, the ice structures accreted around the blade ledge edge were found to have much more complicated shapes under the glaze icing condition (e.g., forming "needle-like" icicles) than those of the rime icing case. Furthermore, the "needle-like" icicle structures accreted around the blade leading edge were found to have a much greater projected area against the incoming airflow, which would intercept more airborne supercooled water droplets to accelerate the ice accretion. As a result, the effective chord length of the iced blade was found to increase nonlinearly, i.e., by 1.5 %, 4.0 %, and 10 % after undergoing 30 s, 60 s, and 120 s of the glaze icing experiment. The fast growth of the very complicated, "needle-like" icicled around the blade leading edge would induce large-scale airflow separations over both the suction and pressure surfaces of the fan blade. Meanwhile, after undergoing 120 s of the glaze icing experiment, the glaze ice structures accreted on the blade was found to block of the airflow passage between the neighbouring blades by 17.6 % and 4.4 % at the blade leading and trailing edges, respectively. As a result, a much faster performance degradation of the fan rotor would be induced by the glaze ice accretion, which was confirmed quantitatively based on air pressure increment measurements across the fan rotor to be de discussed later.

As revealed quantitatively from the measurement results given in Fig. 9(b), the glaze ice layer accreted on the pressure surface at the blade mid-span (i.e., at 50 % span) had a much greater coverage than those at 75 % span. The rapid growth of the "needle-like" icicles at the blade leading edge caused the effective chord length of the iced blade increasing by 8.8 % at the mid-span after 120 s of the glaze icing experiment. The airflow passage between neighbouring blades was blocked by 16.7 % due to the ice accretion. The outer profile of the iced blade was found to deviate from its original shape significantly because of the ice accretion, which would also contribute to the faster performance degradation of the fan rotor under the glaze icing condition.

The ice accretion characteristics near the blade root (e.g., at 25 % span) were found to become very different from those in the outbound regions. Since the unfrozen water collected over the blade surface became much less likely to flow radially because of the smaller centrifugal forces near the blade root, most of the impinged water was found to accumulate within the region near the blade root. No "needle-like" icicles were observed to form in the blade root region. Driven by the aerodynamic shear forces exerted by the incoming airflow, the unfrozen water would be more like to flow along the streamwise direction, causing thicker ice layers near the blade trailing edge than those at the leading edge. While the ice accretion around the blade leading edge near the blade root was found to extend the effective chord length of the iced blade by about 7.8 % after undergoing 120 s of the glaze icing experiment, the ice accretion would also block the airflow passage between the neighbouring blades by about 18 % at the blade leading edge and 11.1 % at the blade trailing edge, respectively.

Fig. 10 shows the variations of the measured NPIR value of the fan rotor as a function of the ice accretion time under the glaze icing condition. In comparison to those under the rime icing condition, the pressure increment of the fan rotor was found to decrease much faster for the glaze icing case. The NPIR value was even found to become negative at the time of $t > 30$ s. Such performance degradation features were correlated well with the characteristics of the glaze icing process described above. Under the combined effects of the centrifugal forces and aerodynamic shear forces, the unfrozen water accumulated on the

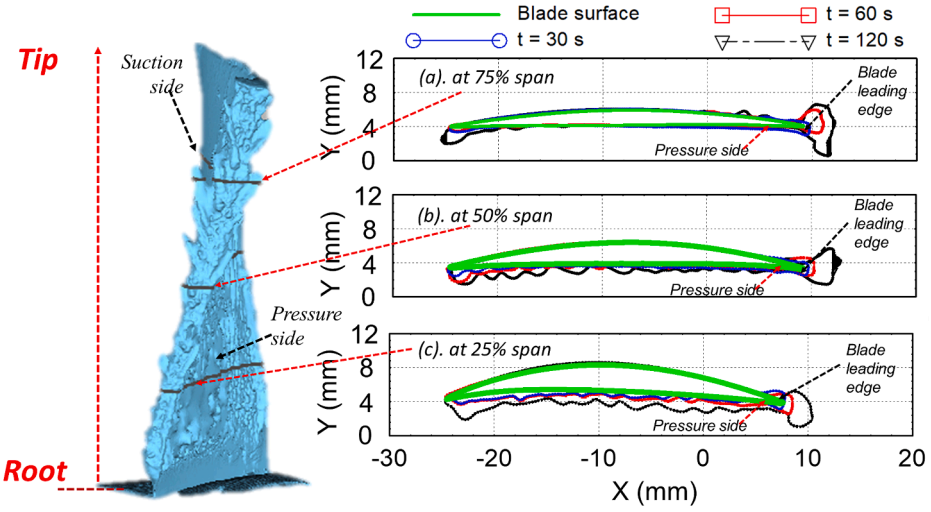

Fig. 9. Extracted profiles of the iced blades at three spanwise locations under the glaze icing condition.

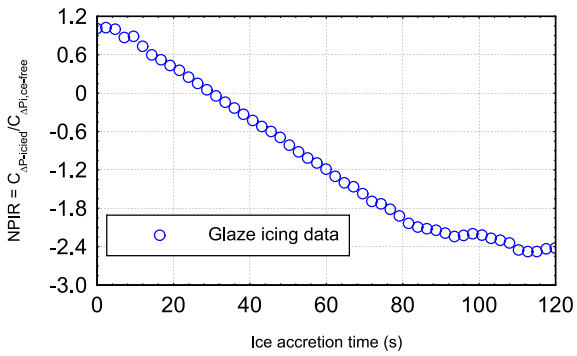

Fig. 10. The measured NPIR value of the fan rotor under the glaze icing condition.

fan blades was found to run back or even take off from the blade surfaces, resulting in the rapid growth of the complex glaze ice structures (e.g., "needle-like" icicles) on the blades. The accreted glaze ice structures with complicated shapes would not only induce massive airflow separations to degrade the aerodynamic performances of the fan blades greatly but also block the air streams from flowing through the fan rotor smoothly. All these factors contributed to the rapid performance degradation of the fan rotor. Therefore, the NPIR value was found to decrease rapidly with the increasing ice accretion time under the glaze icing condition. It should also be noted that the NPIR value was even found to become negative after undergoing 30 s of the glaze icing experiment. It suggests that the glaze ice structures accreted on the fan blades became so detrimental that the fan rotor would not compress the airflow anymore. The iced fan rotor was found to behave like a wind turbine instead, which would extract kinetic energy from the incoming airflow, thereby, causing the air pressure across the fan rotor decrease substantially.

4. Conclusions

An experimental study was conducted to characterize the dynamic ice accretion process on rotating aero-engine fan blades and the resultant performance degradation of the fan rotor under different icing condition. A scaled spinner-fan model was installed in an Icing Research Tunnel and exposed to typical rime and glaze icing conditions. In addition to imaging the dynamic ice accretion process on rotating fan blades, the shape changes of the iced fan blades as a function of the ice accretion time were quantified with a 3D profile scanning system. The air pressure increment across the fan rotor was also monitored during the icing experiments to characterize the performance degradation of the fan rotor induced by the ice accretion.

While supercooled water droplets were found to be frozen into ice instantly upon impinging onto the blade surface under the rime icing condition, the accreted rime ice layers conformed well with the original profiles of the fan blades in general at the initial stage of the icing process. Rime ice structures were found to accumulate on both the suction and pressure sides of the blade surfaces with more ice accretion in the region near the blade roots than those near the blade tips. Interestingly, rime ice accretion was found to be aerodynamically favourable at the initial icing stage, leading to a slight improvement in the fan rotor performance at the beginning of the rime icing process. However, with more and more complex ice structures accreted on the rotating fan blades, the accreted ice structures were found not only to deteriorate the shapes of the deliberately designed blades but also block the airflow passages through the fan rotor substantially (e.g., the thickness of the blade was increased up to 40 %, and blocking up to 14 % of the airflow passage near the blade roots after undergoing 480 s of the rime icing experiment), resulting in a continuous performance degradation of the fan rotor with up to 70 % reduction of the air pressure increment across the fan rotor.

While only a portion of the impinged supercooled water droplets were frozen into ice immediately under the glaze icing condition; the rest of the impinged water was found to stay in liquid and move freely over the ice accreting blade surfaces. Due to the combined effects of the aerodynamic shear forces and centrifugal forces, the unfrozen water was found to run back further downstream and move radially toward the blade tips. In comparison to the rime icing scenario, the accreted glaze ice layers had wider coverages on the blade surfaces. More complex "needle-like" icicles were found to grow rapidly along the blade leading edges, especially in the outbound region, which would induce massive airflow separation over the rotating fan blades. The fast-growing glaze ice structures accreted on the fan blades were found to cause more serious blockage to the airflow passages between the neighbouring blades (e.g., blocking up to 18 % of the airflow passage near the blade roots after 120 s of the glaze icing experiment). As a result, the performance of the iced fan rotor deteriorated so much that the airflow was found to be depressurized, instead of pressurized, after passing the fan rotor. It suggested that the fan rotor behaved like a wind turbine to extract kinetic energy from the incoming airflow, causing the air pressure decrements across the fan rotor after substantial glaze ice accreted on the fan blades.

CRediT authorship contribution statement

Linchuan Tian: Data curation, Formal analysis, Investigation, Writing – original draft. **Haiyang Hu:** Data curation, Formal analysis, Investigation. **Ramsankar Veerakumar:** Data curation, Formal analysis, Investigation. **Hui Hu:** Conceptualization, Formal analysis, Funding acquisition, Methodology, Project administration, Resources, Supervision, Writing – review & editing.

Declaration of competing interest

The authors declare that they have no known competing financial interests or personal relationships that could have appeared to influence the work reported in this paper.

Data availability

Data will be made available on request.

Acknowledgments

The authors want to thank Dr. Linyue Gao, Dr. Yang Liu, Mr. James Benson, and Mr. Andrew Jordan for their help in operating the ISU Icing Research Tunnel Facility. The research work is partially supported by Iowa Space Grant Consortium (ISGC) Base Program for Aircraft Icing Studies. The support of National Science Foundation (NSF) under award numbers of CBET-2313310, CBET-1935363, and CMMI-1824840 is also gratefully acknowledged.

References

[1] M.B. Bragg, A.P. Broeren, L.A. Blumenthal, Iced-airfoil aerodynamics, Prog. Aerosp. Sci. 41 (2005) 323–362, https://doi.org/10.1016/J.PAEROSCI.2005.07.001.
[2] S.E. Campbell, A.P. Broeren, M.B. Bragg, Sensitivity of aircraft performance to icing parameter variations, J. Aircr 44 (2007) 1758–1760.
[3] Y. Cao, W. Tan, Z. Wu, Aircraft icing: an ongoing threat to aviation safety, Aerosp. Sci. Technol 75 (2018) 353–385, https://doi.org/10.1016/j.ast.2017.12.028.
[4] H. Hu, L. Tian, H. Hu, Experimental investigation on ice accretion upon ice particle impacting onto heated surface, AIAA J. (2023) 1–13, https://doi.org/10.2514/1.J062425.
[5] L. Li, Y. Liu, L. Tian, H. Hu, H. Hu, X. Liu, I. Hogate, A. Kohli, An experimental study on a hot-air-based anti-/de-icing system for aero-engine inlet guide vanes, Appl. Therm. Eng. 167 (2020) 114778, https://doi.org/10.1016/j.applthermaleng.2019.114778.

[6] F. Piscitelli, S. Palazzo, F. De Nicola, Icing wind tunnel test campaign on a nacelle lip-skin to assess the effect of a superhydrophobic coating on ice accretion, Appl. Sci. 13 (2023) 5183. https://doi.org/10.3390/APP13085183.
[7] L. Li, Y. Liu, H. Hu, An experimental study on dynamic ice accretion process over the surfaces of rotating aero-engine spinners, Exp. Therm Fluid Sci. 109 (2019) 109879, https://doi.org/10.1016/j.expthermflusci.2019.109879.
[8] L. Tian, L. Li, H. Hu, H. Hu, Experimental study of dynamic ice accretion process over rotating aeroengine fan blades, Https://Doi.Org/10.2514/1.T6667 37 (2022) 353–364. https://doi.org/10.2514/1.T6667.
[9] W.M. Schulze, Aircraft Engine Inlet Cowl Anti-icing System, US Patent: US5088277A, 1988.
[10] Andreas, Linke-Diesinger, Systems of commercial turbofan engines: an introduction to systems functions, Springer (2008).
[11] W. Zhou, Y. Liu, H. Hu, H. Hu, X. Meng, Utilization of thermal effect induced by plasma generation for aircraft icing mitigation, AIAA J. 56 (2018) 1–8, https://doi.org/10.2514/1.J056358.
[12] X. Huang, N. Tepylo, V. Pommier-Budinger, M. Budinger, E. Bonaccurso, P. Villedieu, L. Bennani, A survey of icephobic coatings and their potential use in a hybrid coating/active ice protection system for aerospace applications, Prog. Aerosp. Sci. 105 (2019) 74–97, https://doi.org/10.1016/j.paerosci.2019.01.002.
[13] L. Gray, Review of Aircraft Deicing and Anti-Icing Fluid Storm Water Runoff Control Technologies, in: 2013: p. MANE 6960H01 – Air and Water Pollution Prevention.
[14] R.K. Mcgovern, K. V Bulusu, M. a Antar, H. John, One-dimensional Model of an Optimal Ejector and Parametric Study of Ejector Efficiency, in: 25th International Conference on Efficiency, Cost, Optimization and Simulation of Energy Conversion Systems and Processes (2012) 1–10.
[15] E.S. Reddy, G.H. Abumeri, P.L.N. Murthy, C.C. Chamis, Structural tailoring of aircraft engine blade subject to ice impact constraints, in: 4th Symposium on Multidisciplinary Analysis and Optimization, 1992, 1992. https://doi.org/10.2514/6.1992-4710.
[16] A. Hamed, K. Das, D. Basu, Numerical simulations of ice droplet trajectories and collection efficiency on aero-engine rotating machinery, (2012) 1–10. https://doi.org/10.2514/6.2005-1248.
[17] L. Li, Y. Liu, L. Tian, H. Hu, H. Hu, X. Liu, I. Hogate, A. Kohli, An experimental study on a hot-air-based anti-/de-icing system for aero-engine inlet guide vanes, Appl. Therm. Eng. (2020), https://doi.org/10.1016/j.applthermaleng.2019.114778.
[18] L. Li, Y. Liu, H. Hu, An experimental study on dynamic ice accretion process over the surfaces of rotating aero-engine spinners, Exp. Therm Fluid Sci. (2019), https://doi.org/10.1016/j.expthermflusci.2019.109879.
[19] K. Das, A. Hamed, D. Basu, E. Mechanics, Ice shape prediction for turbofan rotating blades, in: 44th AIAA Aerospace Sciences Meeting and Exhibit, Reno, NV, 2006: pp. 1–12.
[20] K. Das, Numerical simulations of icing in turbomachinery, University of Cincinnati, 2006.
[21] R. Hutchings, Effects of Supercooled Water Ingestion on Engine Performance, 2011.
[22] C.S. Bidwell, Particle Trajectory and Icing Analysis of the E 3 Turbofan Engine Using LEWICE3D Version 3, in: 4th AIAA Atmospheric and Space Environments Conference, 25 - 28 June 2012, New Orleans, Louisiana, 2012: p. AIAA 2012-3037. https://doi.org/10.4271/2011-38-0048.
[23] W. Dong, J.J. Zhu, R. Wang, Y. Chen, Numerical simulation of icing on the rotating blade, in: Proceedings of ASME Turbo Expo 2015: Turbine Technical Conference and Exposition, ASME, Montréal, Canada, 2015: pp. 1–9.
[24] H. Hu, F. Al-Masri, L. Tian, H. Hu, Experimental study of dynamic icing process on a pitot probe model, J Thermophys. Heat Trans (2023) 1–12, https://doi.org/10.2514/1.T6782.
[25] L. Gao, Y. Liu, H. Hu, An experimental investigation on the dynamic glaze ice accretion process over a wind turbine airfoil surface, Int. J. Heat Mass Transf. 149 (2020) 119120, https://doi.org/10.1016/J.IJHEATMASSTRANSFER.2019.119120.
[26] Y. Liu, L. Ma, W. Wang, A.K. Kota, H. Hu, An experimental study on soft PDMS materials for aircraft icing mitigation, Appl. Surf. Sci. (2018), https://doi.org/10.1016/j.apsusc.2018.04.032.
[27] Y. Liu, W. Chen, Y. Peng, H. Hu, An experimental study on the dynamic ice accretion processes on bridge cables with different surface modifications, J. Wind Eng. Ind. Aerodyn. 190 (2019) 218–229, https://doi.org/10.1016/j.jweia.2019.05.007.
[28] Y. Peng, R. Veerakumar, Y. Liu, X. He, H. Hu, An experimental study on dynamic ice accretion and its effects on the aerodynamic characteristics of stay cables with and without helical fillets, J. Wind Eng. Ind. Aerodyn. 205 (2020) 104326, https://doi.org/10.1016/j.jweia.2020.104326.
[29] U.W. Ganz, P.D. Joppa, T.J. Patten, D.F. Scharpf, Boeing 18-inch fan gig broadband noise test, 1998.
[30] L. Tian, L. Li, H. Hu, H. Hu, Experimental study of dynamic ice accretion process over rotating aeroengine fan blades, J. Thermophys. Heat Trans 37 (2023) 353–364, https://doi.org/10.2514/1.T6667.
[31] L. Tian, An experimental study of icing physics and anti-/de-icing techniques for aero-engine icing mitigation, PhD, Iowa State University , 2021. https://dr.lib.iastate.edu/entities/publication/f32658a7-20ee-49c2-9bf9-f4d86d35250d/full (accessed January 28, 2024).
[32] M. Papadakis, A. Rachman, S. Wong, H. Yeong, C.S. Bidwell, Water Droplet Impingement on Simulated Glaze , Mixed , and Rime Ice Accretions, Nasa/Tm-2007-213961 (2007).
[33] Y. Liu, L.J. Bond, H. Hu, Ultrasonic-attenuation-based technique for ice characterization pertinent to aircraft icing phenomena, AIAA J. (2017), https://doi.org/10.2514/1.J055500.
[34] M.K. Politovich, Predicting glaze or rime ice growth on airfoils, J. Aircr. 37 (2000) 117–121, https://doi.org/10.2514/2.2570.
[35] D. Anderson, Acceptable tolerances for matching icing similarity parameters in scaling applications, 39th Aerospace Sciences Meeting and Exhibit (2001). https://doi.org/doi:10.2514/6.2001-832.
[36] K. Zhang, W. Tian, H. Hu, An experimental investigation on the surface water transport process over an airfoil by using a digital image projection technique, Exp. Fluids 56 (2015) 173, https://doi.org/10.1007/s00348-015-2046-z.
[37] R. Veerakumar, L. Gao, Y. Liu, H. Hu, Dynamic ice accretion process and its effects on the aerodynamic drag characteristics of a power transmission cable model, Cold Reg. Sci. Technol. 169 (2020) 102908, https://doi.org/10.1016/j.coldregions.2019.102908.
[38] Y. Liu, H. Hu, An experimental investigation on the unsteady heat transfer process over an ice accreting airfoil surface, Int. J. Heat Mass Transf. 122 (2018) 707–718, https://doi.org/10.1016/j.ijheatmasstransfer.2018.02.023.
[39] L. Ma, Z. Zhang, L. Gao, Y. Liu, H. Hu, Bio-inspired icephobic coatings for aircraft icing mitigation: a critical review, Rev. Adhes. Adhes. 8 (2020) 168–198, https://doi.org/10.7569/RAA.2020.097307.
[40] J. Shin, Characteristics of surface roughness associated with leading-edge ice accretion, J. Aircr. 33 (1996) 316–321, https://doi.org/10.2514/3.46940.